Maximum Power Point Tracking for Wind Turbine Using Integrated Generator–Rectifier Systems

Phuc Huynh, *Student Member, IEEE*, Samira Tungare, and Arijit Banerjee, *Senior Member, IEEE*

***Abstract*—Offshore wind is a rapidly growing renewable energy resource. Harvesting offshore energy requires multimegawatt wind turbines and high efficiency, high power density, and reliable power conversion systems to achieve a competitive levelized cost of electricity. An integrated system utilizing one active and multiple passive rectifiers with a multiport permanent magnet synchronous generator is a promising alternative for an electromechanical power conversion system. Deployment of the integrated systems in offshore wind energy requires maximum power point tracking (MPPT) capability, which is challenging due to the presence of numerous uncontrolled passive rectifiers. This article shows feasibility of MPPT based on a finding that the active-rectifier d-axis current can control the total system output power. The MPPT capability opens up opportunities for the integrated systems in offshore wind applications.**

***Index Terms*—AC–DC power conversion, dc power systems, maximum power point trackers (MPPT), power conversion, rectifiers, wind energy, wind energy generation.**

I. INTRODUCTION

OFFSHORE wind is an emerging renewable energy resource with rapidly increasing installed capacity [2]–[5]. Recently, offshore wind turbines exceeding the common land-based power output have been developed to target a competitive levelized cost of electricity (LCOE). For example, Gamesa 10X [6], Haliade X [7], and Vestas V164 [8] have power ratings ranging between 10 and 12 MW. Development of high-power-density, efficient, and reliable electromechanical power conversion systems for these turbines based on conventional converter topologies is challenging. The major obstacles are limited power-electronics-switch voltage/current ratings and high switching losses [9]. Two-level pulsewidth modulation (PWM) and neutral-point-clamped converters are the most commonly used architectures. The former has a simple construction and a straightforward control scheme [10]–[12]. Each switch is rated for the peak ac-side current and dc-side voltage. Available power electronics devices are connected in series and/or in parallel to process the multimegawatt power. These configurations lead to poor reliability [13]. Neutral-point-clamped topology reduces the voltage rating requirements of each switch [14]–[16]. Loss distribution is uneven across the switches, leading to early failure at the hot spots. Multiport generators have been proposed to reduce the power rating of the individual power converters [17]–[19]. All these architectures rely solely on an active rectifier for ac to dc conversion.

A permanent magnet synchronous generator (PMSG) based integrated generator–rectifier system, as shown in Fig. 1(a), is a promising alternative [20], [21]. The mechanical power on the turbine shaft is converted to ac electrical power by a multiport PMSG. Each port is connected to either a passive or an active rectifier for ac–dc conversion. The dc outputs of the rectifiers are serially connected to form a relatively high-voltage dc bus. Each rectifier supports only a portion of the total dc-bus voltage. Consequently, 60% of the total power is processed on passive rectifiers, leading to a 47% reduction in conversion loss at the rated operating condition. The overall system power density and reliability improve because of the active-rectifier size reduction.

However, power-flow control in the integrated generator–rectifier system is challenging due to the presence of numerous passive rectifiers. The key contribution of this article is to prove that a controllable total dc-bus power flow can be achieved despite having a series string of uncontrolled passive rectifiers. The ability to control the power flow enables maximum power point tracking (MPPT), which is vital in wind-energy applications [10], [22]–[24]. A control framework is proposed based on a relationship between the active-rectifier d-axis current and the total dc-bus power to achieve MPPT. Additionally, filter capacitors at the passive-rectifier outputs are eliminated. The dc-bus voltage ripple is minimized by shifting the corresponding phases of different ac ports feeding the passive rectifiers. MPPT control, along with removal of the bulky filter capacitors, make the integrated generator–rectifier system promising to reduce the offshore-wind LCOE.

The rest of this article is organized as follows. Section II discusses the power-flow control framework for the integrated generator–rectifier system and applies this methodology for MPPT. Simulation and experimental results are presented in Sections III and IV, respectively, to corroborate the findings. Finally, Section V concludes this article.

Manuscript received December 18, 2019; revised April 30, 2020; accepted June 8, 2020. Date of publication June 14, 2020; date of current version September 4, 2020. This work was supported in part by the Advanced Research Projects Agency-Energy (ARPA-E), U.S. Department of Energy, under Award DE-AR0001057, and in part by the Grainger Center for Electric Machinery and Electromechanics. This paper was presented at the 11th Annual IEEE Energy Conversion Congress and Exposition, Baltimore, Maryland, USA, September 29–October 3 2019 [1]. Recommended for publication by Associate Editor Y. A.-R. I. Mohamed. *(Corresponding author: Phuc Huynh.)*

The authors are with the Electrical and Computer Engineering, University of Illinois at Urbana–Champaign, Urbana, IL 61801 USA (e-mail: pthuynh2@illinois.edu; samirat2@illinois.edu; arijit@illinois.edu).

Color versions of one or more of the figures in this article are available online at https://ieeexplore.ieee.org.

Digital Object Identifier 10.1109/TPEL.2020.3002254

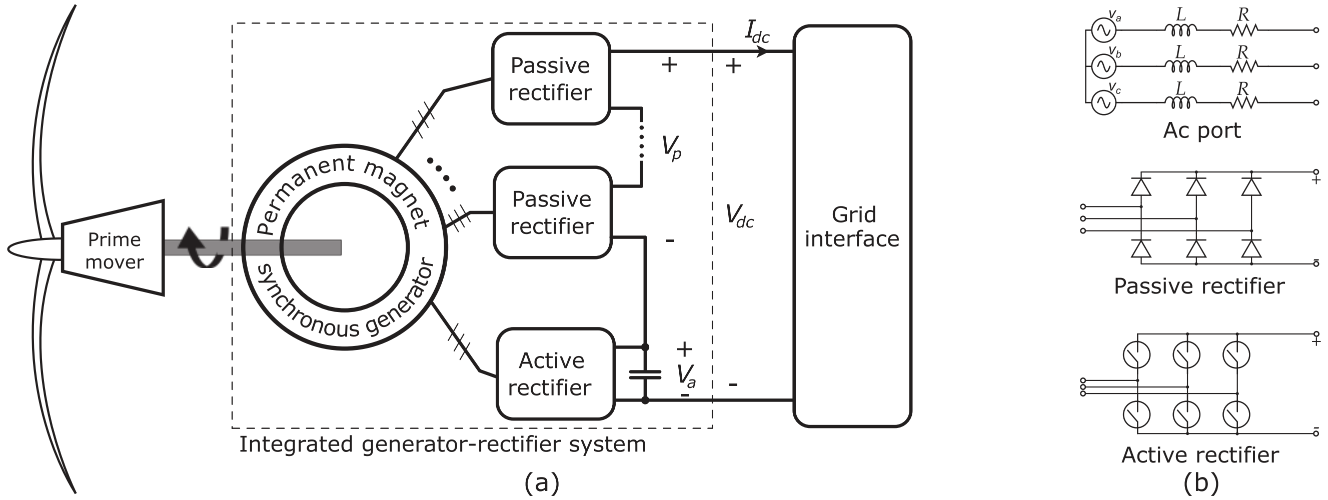

Fig. 1. (a) Wind turbine power-point tracking architecture: the prime mover is a variable-speed wind turbine. The turbine shares a common shaft with the multiport PMSG. AC power is converted to dc by an integrated generator–rectifier system. The dc output is connected to a stiff dc interface. The integrated generator–rectifier system performs maximum power-point tracking to extract the turbine maximum power. (b) Each phase of a three-phase ac port is modeled by a back EMF source in series with generator inductance L and phase resistance R. The passive rectifier is a six-pulse diode rectifier, and the active rectifier is a three-phase two-level converter.

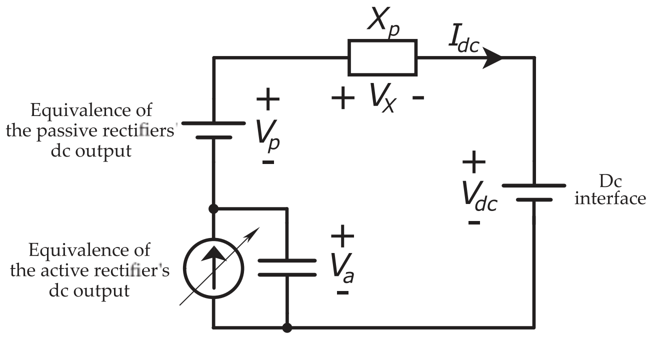

Fig. 2. Simplified equivalent circuit of the integrated generator–rectifier system. The dc output of the passive rectifiers is modeled by a voltage source. The output of the active rectifier is modeled by a controllable current source. The serial voltage and current sources are connected to a constant dc voltage representing the dc interface.

II. Power-Flow Control for the Integrated Generator–Rectifier System

This section develops the power-flow control framework for the proposed integrated generator–rectifier system. The system dc output is assumed to be connected to a stiff dc interface. This assumption is valid for both ac and dc collection grids [9]. For the ac case, the interface is an intermediate dc bus that is regulated by a grid-side converter. For the dc case, the dc voltage is controlled by a converter at the dc-grid substation [25], [26].

A simplified equivalent circuit of the integrated system is shown in Fig. 2. The total output of the passive rectifiers is modeled as a generator-speed-dependent voltage source, denoted by V_p, in series with a commutation reactance, denoted by X_p. By ensuring a phase shift among different ac ports, the voltage ripple of the total passive-rectifier output can be neglected, as detailed in Section II-A. The active-rectifier dc-side voltage, denoted by V_a, is determined by the difference between the constant grid interface voltage, V_{dc}, and the passive-rectifier output voltage. The controllable power drawn by the active rectifier determines its dc-side current. The active rectifier is modeled by a controllable current source. Due to the series connection, the current flowing out of the active rectifier determines the amount of power flowing into the dc bus, as detailed in Section II-B. Cascaded proportional-integral (PI) controllers are proposed for practical implementation. The power-flow control framework is applied to perform MPPT in Section II-C.

A. *Passive-Rectifier Voltage-Ripple Minimization*

Considering a PMSG with k three-phase ac ports, $(k-1)$ ports power passive rectifiers with no output filter capacitors. The dc-output voltage ripple of each passive rectifier has a peak every $\frac{\pi}{3}$ radians, as shown in Fig. 3(a). Serial connection of the dc outputs with an appropriate phase shift leads to a minimal voltage ripple percentage, defined as the ratio between the peak-to-peak ripple and the average value. For example, the ripple percentage of two passive rectifiers with $\frac{\pi}{6}$ phase shifting is 3%, compared to 14% without phase shifting, as shown in Fig. 3(b). In general, a phase shift of $\frac{\pi}{3(k-1)}$ radian minimizes the voltage ripple for a system with $(k-1)$ passive rectifiers. Increasing the number of ac ports reduces the voltage ripple percentage but at a diminishing rate, as shown in Fig. 3(c). This technique is similar to the use of multipulse diode rectifiers and phase-shifting transformers in high-power drives to reduce the line-current harmonic distortion [27].

Assuming a negligible voltage ripple and a constant dc-bus current I_{dc}, the total dc output voltage of $(k-1)$ passive rectifiers at the electrical frequency ω is

$$V_{\text{passive}} = \underbrace{\frac{3}{\pi}(k-1)\sqrt{3}E(\omega)}_{V_p} - \underbrace{(k-1)\left(\frac{3}{\pi}\omega L + 2R\right)I_{\mathrm{dc}}}_{V_X} \tag{1}$$

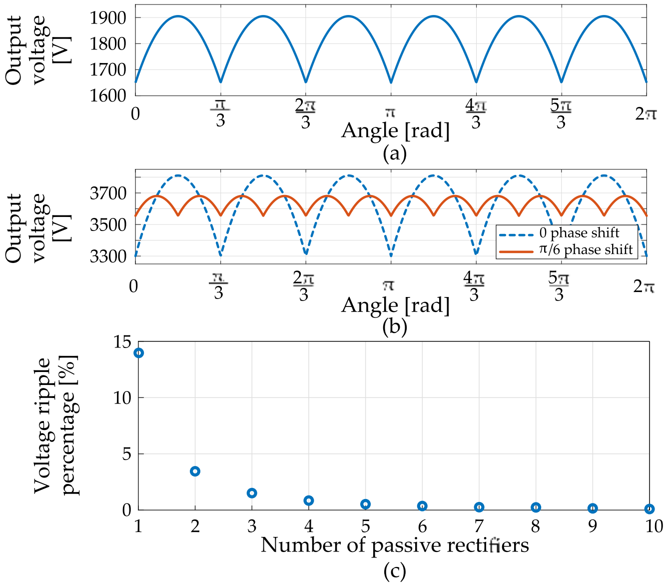

Fig. 3. Example output voltage waveforms from the integrated system in Fig. 1 with each ac port generating 1.1 kV peak line-to-neutral voltage at 20 Hz electrical frequency. (a) DC output voltage of one passive rectifier. (b) DC output voltage of two passive rectifiers connected in series with/without phase shifting between the corresponding ac ports. (c) Ratio between the voltage V_p peak-to-peak ripple and the average value is reduced as the number of passive ports is increased.

where L and R are the synchronous inductance and per-phase equivalent series resistance of each ac port, respectively [28]. The back EMF $E(\omega)$ is electrical-frequency-dependent

$$E(\omega) = \frac{\omega}{2\pi f_0}E_0 \quad (2)$$

where f_0 and E_0 are the rated electrical frequency and the rated line-to-neutral peak back EMF, respectively, of each ac port. The term V_X captures effects of the synchronous inductance, the phase resistance, and the dc-bus current on the dc-side voltage of the passive rectifier. The synchronous inductance is assumed to be sufficiently low such that the duration of phase current commutation is less than one-sixth of the electrical period, corresponding to Mode I operation of a conventional six-pulse diode bridge rectifier [28].

B. Power-Flow Control Using the Active Rectifier

The next step is to derive a relationship between the active-rectifier ac-side current and the dc-bus power. Neglecting the conversion losses in the active rectifier, the power balance between the ac and the dc sides leads to

$$\frac{3}{2}E(\omega)I_{sd} - \frac{3}{2}I_{sd}^2R = V_aI_{\rm dc} \quad (3)$$

where V_a is the active-rectifier dc-side voltage and I_{sd} is the d-axis component of the active-rectifier ac-side current. The d-axis is aligned with the peak phase-A back EMF. Using Fig. 2

$$V_a = V_{\rm dc} - V_p + X_pI_{\rm dc}. \quad (4)$$

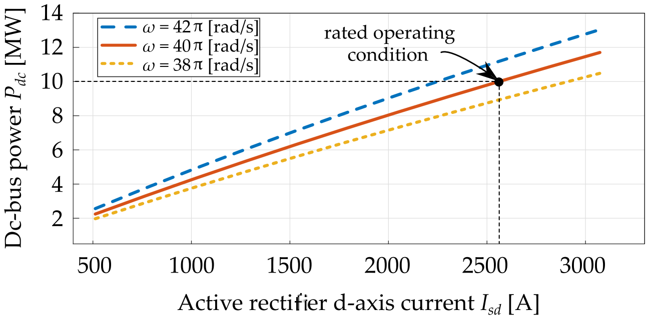

Fig. 4. At each generator speed, the power drawn from the integrated generator–rectifier system depends on the active-rectifier d-axis current.

The dc-bus current is represented by

$$I_{\rm dc} = \frac{P_{\rm dc}}{V_{\rm dc}} \quad (5)$$

where $P_{\rm dc}$ is the dc-bus power. Substituting (4) and (5) in (3), the dc-bus power relates to the active-rectifier d-axis current by

$$\frac{3}{2}E(\omega)I_{sd} - \frac{3}{2}I_{sd}^2R = P_{\rm dc}^2\left((k-1)\frac{1}{V_{\rm dc}^2}\left(\frac{3}{\pi}\omega L + 2R\right)\right) + P_{\rm dc}\left(1 - \frac{3}{\pi}(k-1)\frac{\sqrt{3}E(\omega)}{V_{\rm dc}}\right). \quad (6)$$

Equation (6) signifies that the active-rectifier d-axis current can control the power flowing into the dc-bus, or, equivalently, the power drawn from the turbine.

Fig. 4 illustrates the relationship between I_{sd} and $P_{\rm dc}$ using a 10 MW wind-turbine system based on a three-port PMSG. Each port has a rated back EMF of 1.1 kV at 20 Hz electrical frequency, an equivalent series resistance of 12 mΩ and a synchronous inductance L of 0.47 mH. These values correspond to 0.02 p.u. resistance and 0.1 p.u. synchronous reactance, respectively, at the rated operating condition. The relationship is also demonstrated at two other electrical frequencies to show the possibility of using power control for generator-speed regulation.

Power-flow control is achieved by using a cascaded architecture, as illustrated in Fig. 5. The inner loop comprises current controllers to regulate the d-axis and q-axis currents of the active rectifier. The d-axis and q-axis current control the power flow and power factor, respectively. The outer-loop power controller calculates the d-axis current command to deliver the reference power $P_{\rm dc}^*$ to the dc bus. The power command is the output of an MPPT algorithm that uses generator rotational speed as an input. Setting the q-axis current to zero leads to a unity power-factor operation of the active rectifier.

The current controllers are designed based on the ac-port current dynamics in the dq reference frame given by

$$L\frac{dI_{sd}}{dt} = -RI_{sd} + \omega LI_{sq} + E - V_{rd} \text{ and} \quad (7)$$

$$L\frac{dI_{sq}}{dt} = -RI_{sq} - \omega LI_{sd} - V_{rq} \quad (8)$$

where V_{rd} and V_{rq} are the input d-axis and q-axis voltages, respectively. The d-axis is aligned with the peak phase-A

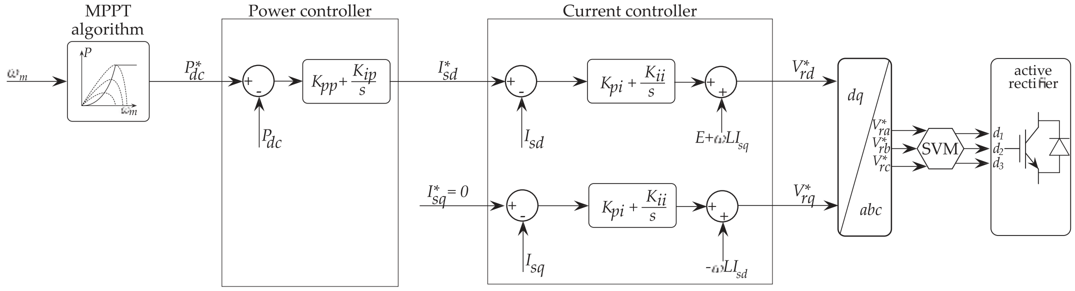

Fig. 5. Cascaded architecture applied to the active rectifier to accomplish power-flow control for the entire integrated generator–rectifier system.

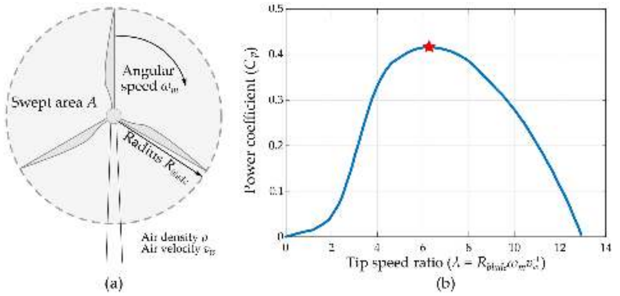

Fig. 6. (a) Illustration of a three-bladed wind turbine. (b) Typical wind-turbine power coefficient versus tip-speed ratio curve [29].

back EMF. The q-axis leads the d-axis by 90°. Using (7), a PI controller with feed-forward terms is chosen to generate the d-axis voltage command

$$V^*_{rd} = K_{pi}(I^*_{sd} - I_{sd}) + \int K_{ii}(I^*_{sd} - I_{sd})dt + E + \omega_0 LI_{sq} \tag{9}$$

where I^*_{sd}, K_{ip}, and K_{ii} are the reference d-axis current, the proportional, and integral gains, respectively. Using (8), the q-axis current controller can be designed similarly.

Precise prior knowledge of L and R allows direct calculation of the d-axis current command for a required power demand using (6). The impact of any parametric uncertainties on the power flow control can be minimized by using an outer-loop PI control, given by

$$I^*_{sd} = K_{pp}(P^*_{\mathrm{dc}} - P_{\mathrm{dc}}) + K_{ip}\int (P^*_{\mathrm{dc}} - P_{\mathrm{dc}})dt \tag{10}$$

where K_{pp} and K_{ip} are the proportional and integral gains, respectively.

C. MPPT Using Integrated Generator–Rectifier System

The proposed power-control architecture is applied to track the wind turbine maximum power point. MPPT is achieved if at each generator speed, the electrical power drawn follows the maximum power curve [23]. Consider a wind turbine in Fig. 6 with $R_{\text{blade}} = 164$ m, operating at a rated wind speed of 12 m/s and an air density ρ of 1.15 kg/m^3. Fig. 7 plots the mechanical power curves of the wind turbine at various wind speeds using dashed lines. The maximum power curve is formed by connecting peak values of all the mechanical power curves.

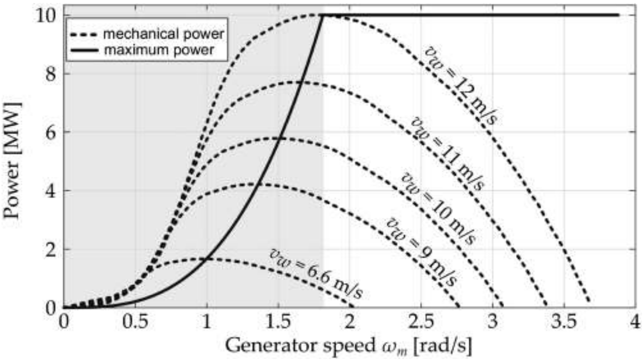

Fig. 7. Mechanical power curves and maximum power curve of a 10 MW wind turbine.

Consider the operation at a wind speed of 12 m/s. The vertical line crossing the intersection between the maximum power curve and the mechanical power curve splits the graph into two regions. In the gray region, the input mechanical power to the generator is higher than the output electrical power. The generator rotational speed increases. Then, the generator enters the white region, in which the mechanical power is lower than the electrical power. The generator slows down. Eventually, the speed settles at the border of the two regions, at which point the maximum power of 10 MW is generated.

III. SIMULATION RESULTS

A. Power-Flow Control

Fig. 8 shows the simulation model including the power electronics switching events for verifying the relationship between the d-axis current and the dc-bus power, as in (6). A three-port PMSG is modeled by three voltage sources in series with resistance and inductance. The frequency and amplitude of the voltage sources are dependent on an external reference-speed signal. Parameters of each port follow the values given in Section II-B. Port-1 and -2 are connected to three-phase diode rectifiers. The phase-A voltages (and also Phase-B and -C) of these two ports are shifted by $\frac{\pi}{6}$ electrical radian from each other to minimize the voltage ripple on the passive rectifiers' dc output. Port-3 powers an insulated-gate bipolar transistor (IGBT)-based active rectifier that switches at 2 kHz. The rectifier outputs are serially connected to form the dc bus. The dc-bus voltage is maintained at 5.7 kV to represent the grid interface.

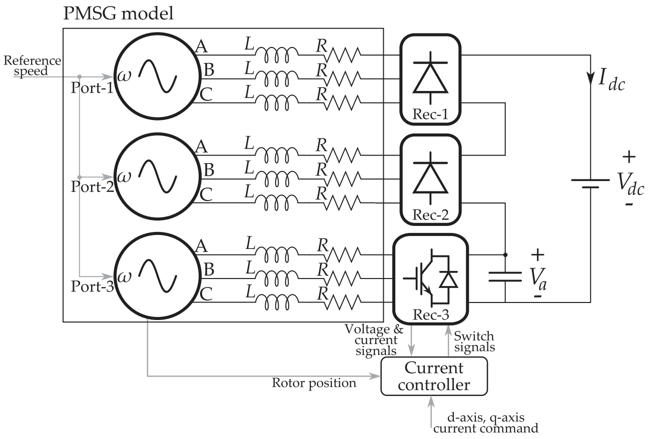

Fig. 8. Simulation model based on a three-port PMSG with integrated power electronics used to illustrate the drive-train operation at different generator speeds.

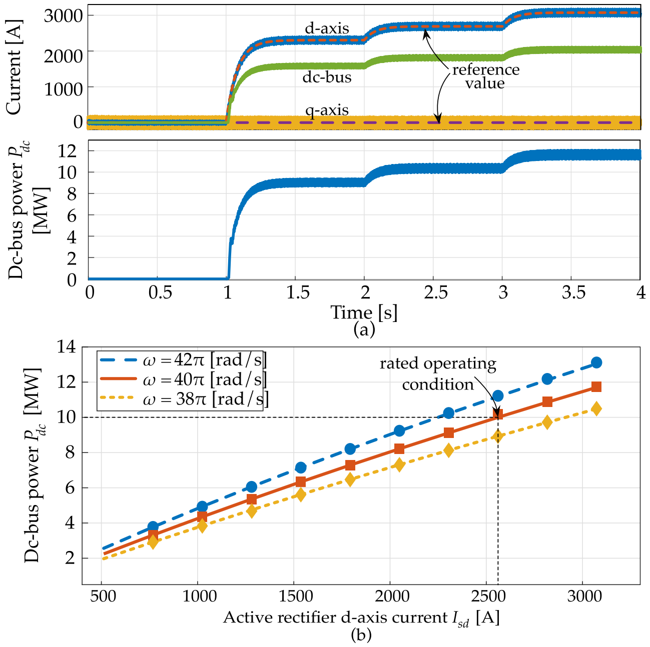

Fig. 9. (a) (Top plot) Active-rectifier d-axis and q-axis currents track the reference command, presented by the dotted lines. The dc-bus current varies accordingly by changing the d-axis current, leading to a change in the dc-bus power (bottom plot). (b) Relationship between dc-bus power and active-rectifier d-axis current acquired from the simulation model (recorded by the markers) matches the theoretical analysis [plotted by the lines using (6)].

Fig. 9(a) illustrates that the active-rectifier d-axis current is the control input for the dc-bus power. The upper plot shows the current waveforms corresponding to different active-rectifier d-axis current reference values, when the q-axis current is commanded to stay at zero. The dc-bus current follows the d-axis current. The dc-bus power varies proportionally to the dc-bus current, as shown by the bottom plot of Fig. 9(b).

Verification of the theoretical analysis, (6), is shown in Fig. 9(b). Different dc-bus power values are recorded at generator speeds $\omega = 38\pi, 40\pi$, and 42π rad/s, while the d-axis current takes values ranging from 500 to 3100 A. The recorded dc-bus power is plotted versus the d-axis current using the diamond, square, and circle markers. For each ω, (6) is used to predict the dc-bus power and shown by dotted, solid, and dashed curves.

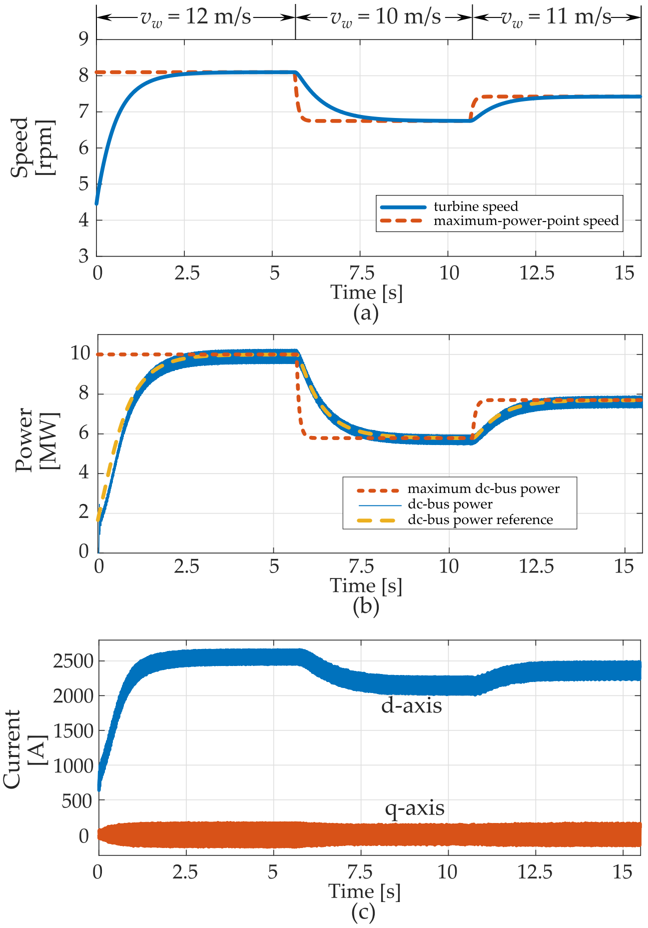

Fig. 10. Waveforms to illustrate the system MPPT capability. (a) At each wind speed, the turbine speed (solid-blue line) successfully tracks the optimal speed to generate maximum power. (b) DC-bus power and the turbine mechanical power versus time. (c) d-axis and q-axis currents to achieve MPPT.

B. MPPT Illustration

The simulation model presented in Fig. 9(a) is used to illustrate the application of the proposed integrated generator–rectifier system to achieve MPPT. The reference speed to the generator is the rotational speed ω_m of a wind turbine with dynamics

$$J\omega_m \frac{d\omega_m}{dt} = P_{\text{turbine}} - P_{\text{dc}} \tag{11}$$

where J is the wind-turbine moment of inertia, chosen to be 28.7×10^6 kg $\cdot$ m^2. To reduce the simulation run time, this value was selected to be 50 times lower than a representative value for a 10 MW turbine [30]. For each wind speed, the turbine power P_{turbine} follows the mechanical power curve in Fig. 7. Taking the turbine rotational speed as the feedback signal, the MPPT algorithm in Fig. 5 sets the power controller reference value to follow the maximum-power curve in Fig. 7.

Fig. 10 shows that the proposed integrated generator-rectifier architecture tracks the wind-turbine maximum power point.

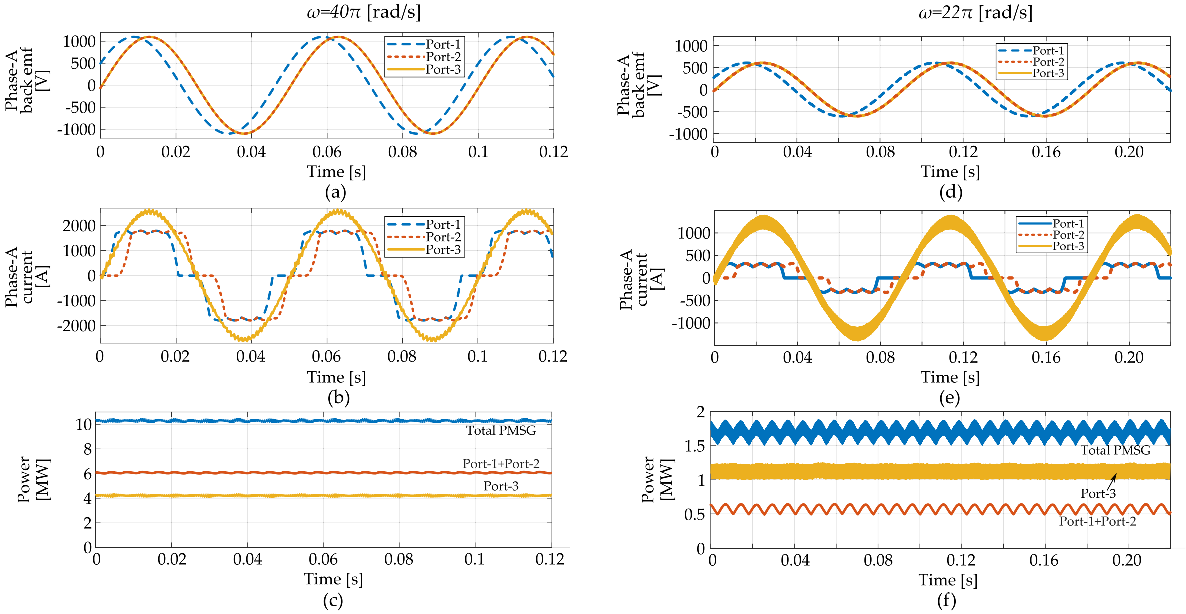

Fig. 11. Generator phase-A back EMF, phase-A current, and power of the passive and active rectifiers at different operating speeds. (a) Sinusoidal and phase-shifted back EMFs at the rated generator speed. (b) Corresponding phase-A currents. (c) Sharing of PMSG input power between ac ports powering active versus passive rectifiers. (d) Back EMFs at the minimum operating speed that is equal to 55% the rated speed. (e) Phase-A currents corresponding to the minimum speed. (f) Power sharing between the ac ports powering active and passive rectifiers at the minimum operating speed.

At time zero, the turbine rotates at 55% of the rated speed and the wind speed is 12 m/s. The turbine maximum power is 10 MW while the dc bus is commanded to draw 2 MW. As the turbine speed increases [following the solid-blue line in Fig. 10(a)], the MPPT algorithm boosts the power command sent to the power controller, shown by the dotted-orange line in Fig. 10(b). Eventually, the electrical power equals the maximum power, allowing the wind turbine settle to the optimal speed, at which point 10 MW is extracted. The corresponding d-axis and q-axis currents are shown in Fig. 10(c).

This operation is also illustrated in Fig. 10 at varying wind-speed conditions. At instances 5.5 and 10.5 s, the wind speed changes to 10 and 11 m/s, respectively. In response to the wind-speed variation, the MPPT controller varies its power command, shown by the dashed-yellow line in Fig. 10(b). The dc-bus power tracks the reference power, allowing the turbine to rotate at the optimal speed for maximum power extraction.

C. PMSG Power Quality and Torque Ripple Assessment

This section quantifies the impacts of the distorted ac currents due to the diode-bridge operation on the total PMSG power quality as well as estimates the generator torque ripple.

Fig. 11(a) shows the phase-A back EMFs corresponding to Port-1, Port-2, and Port-3 at the 20-Hz rated electrical frequency. At 10-MW rated power drawn by the dc-bus, the phase-A currents of the three ac ports are shown in Fig. 11(b). The currents corresponding to the diode bridges are nonsinusoidal, as expected. The total PMSG input power is calculated by adding instantaneous power output of all the back EMF sources, as shown in Fig. 11(c). The total input power is slightly greater than 10 MW to account for the generator resistive losses. 60% of the total power is processed by the passive rectifiers connected to Port-1 and Port-2. The ripple factor, defined as the ratio between ripple-power rms value and the dc power value, is used to quantitatively assess the input power ripple. At the rated condition, the ripple factor is 0.4%.

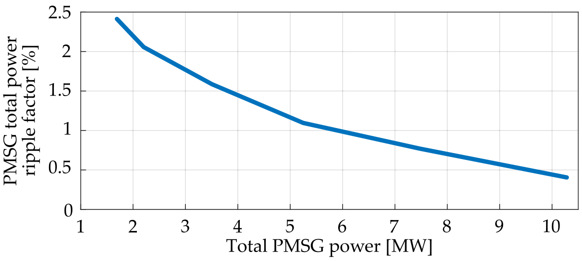

Fig. 12. Ripple factor of the total PMSG power is always below 2.5% and decreases as the output power increases.

Operation at the minimum generator speed is considered next to evaluate the ripple factor variation as a function of the generator input power. The back EMF amplitude and frequency are proportional to the generator speed. Therefore, both decrease for a minimum operating speed that equals to 55% of the rated value, as shown in Fig. 11(d). The ac-port currents vary, as illustrated in Fig. 11(e), to deliver the amount of power shown in Fig. 11(f). For a wind turbine, the input power is proportional to the cube of the generator speed [23], resulting in the input power to be 1.7 MW at the minimum operating speed. Unlike Fig. 11(c), majority of the power is processed by the active rectifier connected to Port-3, as shown in Fig. 11(f). The ripple factor is 2.4%. Fig. 12 shows the ripple factor for the entire operating speed range as a function of the input power. Due to high inertia of a wind turbine, the mechanical speed can

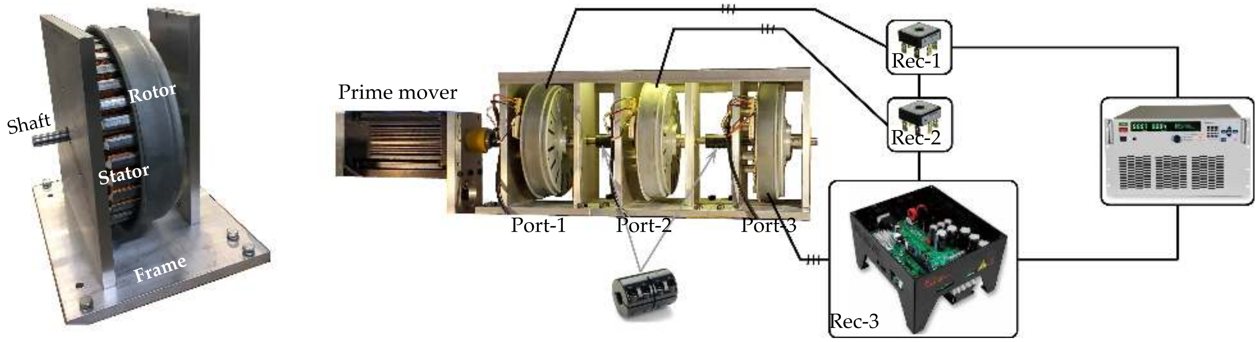

(a) (b)

Fig. 13. Experimental setup. (a) Single ac port assembly. (b) Three ac-port assemblies are joined using couplers, allowing phase shifting between ports. Port-1 feeds the active rectifier while Port-2 and Port-3 power passive rectifiers. DC outputs are serially stacked and connected to a constant dc bus maintained by an electronic load operating in constant voltage mode. Note that the PMSG setup is used only to validate the phase-shifting concept and does not reflect a real PMSG design for off-shore wind.

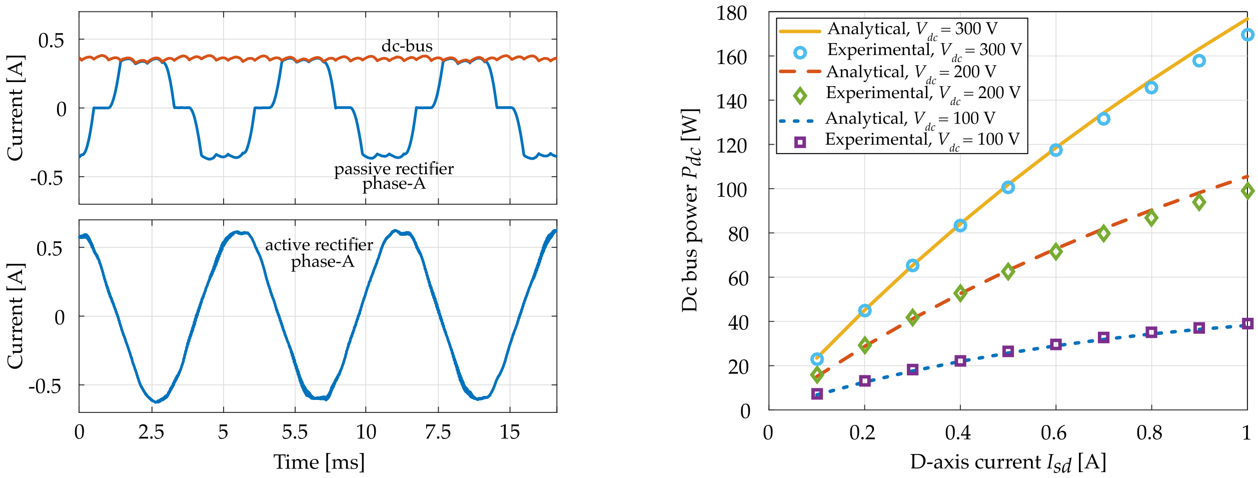

(a) (b)

Fig. 14. (a) Current waveforms from the experimental setup: (top) phase current of Port-1, feeding the passive rectifier, and dc-bus current, (bottom) phase current of Port-3, feeding the active rectifier. The power factor at the passive rectifier is 0.91 and at the active rectifier is 1. (b) Theoretical relationship between the active-rectifier d-axis current and the dc-bus power is validated by experimental measurements. The lines illustrate the theoretical predictions in (6), while the experimental measurements are recorded by the discrete markers.

be considered to be relatively constant within the time scale of the electrical dynamics. Consequently, this power ripple is equivalent to the torque ripple. The integrated generator–rectifier system exhibits a ripple factor lower than the acceptable level of 5%–10% [31], [32].

IV. EXPERIMENTAL RESULTS

A. Experimental Setup

The multiport generator is experimentally emulated using three Samsung DC96-01218D PM machines with three phases and 48 poles, as shown in Fig. 13. The machine assembly is shown in Fig. 13(a). Each phase has an equivalent series resistance of 2 Ω and an equivalent series inductance of 6.5 mH, measured at 60 Hz. The machine produces a sine-wave back EMF with a back EMF constant 0.131 V(peak line to neutral)/r/min.

Three ac-port assemblies, named Port-1, Port-2, and Port-3, are axially joined using shaft couplers to form a generator, as shown in Fig. 13(b). The couplers allow free adjustment of the rotor relative angular position, resulting in a phase-shifted back EMF between different ac ports. A $\frac{\pi}{6}$ electrical radian phase shift is created between Port-1 and Port-2 to minimize the dc-bus voltage ripple. The setup illustrates just the phase-shifting concept using off-the-shelf components, and does not reflect a real multiport PMSG design for off-shore wind. A real generator could be designed to integrate multiple ports inside a single generator body [33], [34].

Port-1 and Port-2 feed passive rectifiers MT3516 A. DC outputs of the rectifiers are serially stacked to form a dc bus. Port-3 powers the active rectifier Rec-3, made from a Texas Instruments High Voltage Motor Controller and PFC Developer's Kit. The dc bus is regulated by the electronic load Magna Power ARx operating in constant voltage mode. The PMSG is driven by a programmable prime mover that can operate in constant speed, constant torque, or wind-turbine emulator mode.

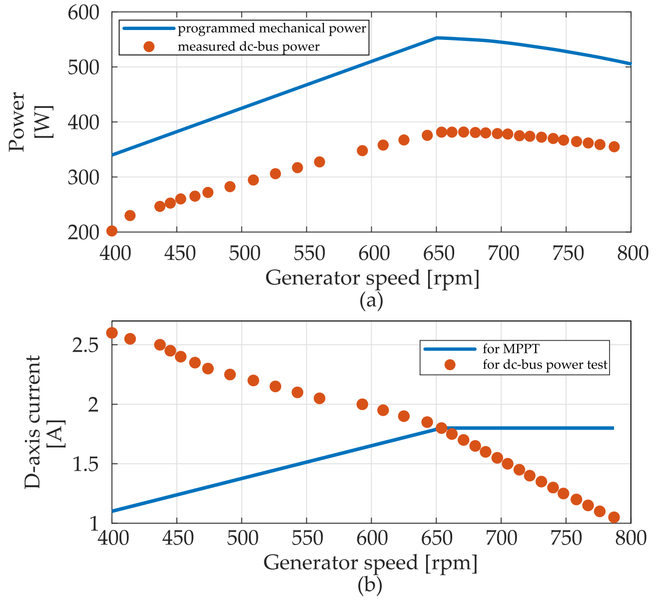

Fig. 15. Power characteristics of the wind turbine. (a) Amount of power delivered to the dc-bus has a peak value of 381 W at a generator speed of 656 r/min. (b) Power is experimentally measured by applying a torque profile following the dotted-orange line. The solid-blue curve is used to achieve MPPT.

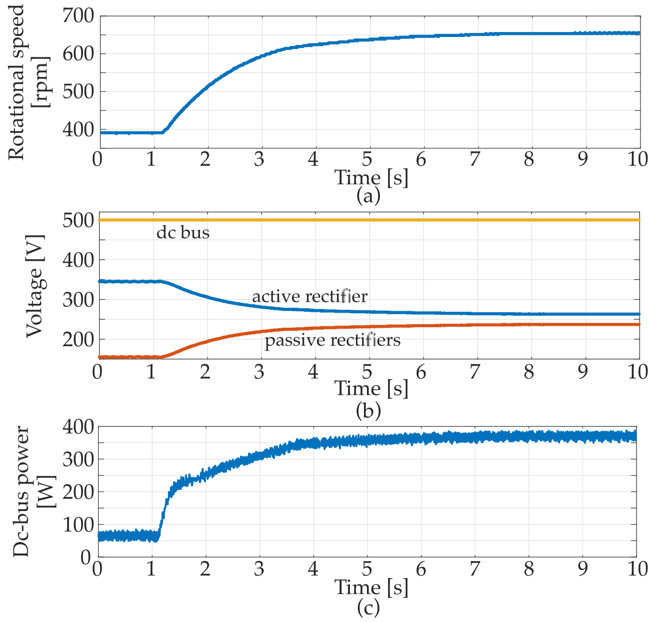

Fig. 16. Waveforms of the MPPT operation. (a) Turbine starts at 391 r/min and settles at 650 r/min, the speed for maximum power generation. (b) Passive-rectifier dc-side voltage increases as the rotational speed increases. The active-rectifier dc-side voltage behave oppositely. The dc-bus voltage is constant at all the rotational speed. (c) DC-bus power successfully track the maximum value of 381 W.

B. DC-Bus Power—Active-Rectifier Current Relationship

The relationship between the active-rectifier d-axis current and the dc-bus power is validated experimentally. A prime mover operating in speed-regulation mode drives the generator at three operating points: 150, 300, and 450 r/min. These three values correspond to dc-bus voltages of 100, 200, and 300 V, respectively, to be maintained by the electronic load. The dc-bus voltages are chosen to be the minimum values that ensure controllability of the active rectifier, i.e., the sum of the maximum open-circuit line-to-line back emf of all the ac ports. Although a higher dc-bus voltage is possible, the resulting volt-ampere rating requirement on the active rectifier would be increased [20].

Fig. 14(a) shows the active, passive, and dc-bus current waveforms. The active rectifier drives sinusoidal current out of Port-3. The phase currents of Port-1 (and also Port-2) are nonsinusoidal, as expected due to operation of the passive rectifier. The current flowing to the dc-bus is constant with a low ripple due to the phase shift between Port-1 and Port-2. Fig. 14(b) validates the theoretical and experimental relationship between the d-axis current and the dc-bus power. Theoretical values are predicted by (6). The dc-bus power is measured at the output of the generator set.

C. MPPT Validation

The prime mover is programmed to emulate a wind turbine with mechanical power characteristics shown by the solid blue curve in Fig. 15(a). The amount of electrical power extractable at the dc-bus, shown by the orange dots, is lower than the programmed values due to the power-train losses, approximately 35%. These experimental measurements are achieved by setting the active-rectifier d-axis current to the values of the orange dots in Fig. 15(b). The maximum power point is tracked by utilizing the d-axis current profile versus the rotational speed shown by the solid blue line in Fig. 15(b). The intersection at the speed corresponding to the maximum power point ensures MPPT.

Fig. 16 illustrates the waveforms of the MPPT operation. Before 1.2 s, the prime mover rotates at a constant 391 r/min. At 1.2 s, the prime mover enters the turbine emulator mode. The generator speeds up and eventually settles at 656 r/min, as shown in Fig. 16(a). Fig. 16(b) shows the passive-rectifier voltage increasing with the rotational speed. Meanwhile, the active-rectifier dc-side voltage is reduced due to a constant dc-bus voltage. At the optimal rotational speed, the dc-bus power is 381 W, coinciding with the maximum power point shown in Fig. 15.

V. CONCLUSION

This article presents an MPPT methodology for an integrated generator–rectifier system. An analytical relationship between the dc-bus power and the active-rectifier d-axis current is established and validated using both simulation and experiment. A cascaded control architecture is proposed for practical implementation. The inner loop comprises PI current controllers with feed-forward terms, while the outer loop is a PI power controller. The satisfactory power tracking performance has been accomplished. The power flow control enables the wind turbine MPPT through controlling the dc-bus power. This capability opens up opportunities for the integrated generator–rectifier systems in wind energy applications.

REFERENCES

[1] P. Huynh, S. Tungare, and A. Banerjee, “Maximum power point tracking for wind turbine using integrated generator-rectifier systems,” in *Proc. IEEE Energy Convers. Congr. Expo.*, Sep. 2019, pp. 13–20.

[2] D. S. Ottensen, “Global offshore wind market report,” Norweigian Energy Partner, Oslo, Norway, Tech. Rep. 02092019, 2018.

[3] C. Bak *et al.*, “Light rotor: The 10-MW reference wind turbine,” in *Proc. Eur. Wind Energy Conf. Exhib.*, 2012, pp. 1–10.

[4] P. Higgins and A. Foley, “The evolution of offshore wind power in the united kingdom,” *Renewable Sustain. Energy Rev.*, vol. 37, pp. 599–612, 2014.

[5] W. Musial, P. Beiter, P. Spitsen, J. Nunemaker, and V. Gevorgian, “2018 offshore wind technologies market report,” National Renewable Energy Laboratory, Golden, CO, Canada, Tech. Rep., Aug. 9, 2019. [Online]. Available: https://www.energy.gov/eere/wind/downloads/2018-offshore-wind-market-report

[6] Siemens Gamesa, “SG 10.0-193DD Offshore wind turbine,” Jan. 16, 2019. [Online]. Available: https://www.siemensgamesa.com/en-int/products-and-services/offshore/wind-turbine-sg-10-0-193-dd

[7] GE Renewable Energy, “Haliade-X 12 MW offshore wind turbine platform,” Sep. 19, 2019. [Online]. Available: https://www.ge.com/renewableenergy/wind-energy/offshore-wind/haliade-x-offshore-turbine

[8] MHI Vestas Offshore Wind, “The world’s most powerful available wind turbine gets major power boost,” Dec. 4, 2017. [Online]. Available: http://www.mhivestasoffshore.com/worlds-most-powerful-available-wind-turbine-gets-major-power-boost/

[9] V. Yaramasu, B. Wu, P. C. Sen, S. Kouro, and M. Narimani, “High-power wind energy conversion systems: State-of-the-art and emerging technologies,” *Proc. IEEE*, vol. 103, no. 5, pp. 740–788, May 2015.

[10] M. Chinchilla, S. Arnaltes, and J. C. Burgos, “Control of permanent-magnet generators applied to variable-speed wind-energy systems connected to the grid,” *IEEE Trans. Energy Convers.*, vol. 21, no. 1, pp. 130–135, Mar. 2006.

[11] J. Lu, S. Golestan, M. Savaghebi, J. C. Vasquez, J. M. Guerrero, and A. Marzabal, “An enhanced state observer for dc-link voltage control of three-phase AC/DC converters,” *IEEE Trans. Power Electron.*, vol. 33, no. 2, pp. 936–942, Feb. 2018.

[12] N. He, M. Chen, J. Wu, N. Zhu, and D. Xu, “20-kW zero-voltage-switching SiC-mosfet grid inverter with 300 kHz switching frequency,” *IEEE Trans. Power Electron.*, vol. 34, no. 6, pp. 5175–5190, Jun. 2019.

[13] F. Blaabjerg, M. Liserre, and K. Ma, “Power electronics converters for wind turbine systems,” *IEEE Trans. Ind. Appl.*, vol. 48, no. 2, pp. 708–719, Mar. 2012.

[14] N. Celanovic and D. Boroyevich, “A comprehensive study of neutral-point voltage balancing problem in three-level neutral-point-clamped voltage source PWM inverters,” *IEEE Trans. Power Electron.*, vol. 15, no. 2, pp. 242–249, Mar. 2000.

[15] A. Yazdani and R. Iravani, “A neutral-point clamped converter system for direct-drive variable-speed wind power unit,” *IEEE Trans. Energy Convers.*, vol. 21, no. 2, pp. 596–607, Jun. 2006.

[16] A. Nabae, I. Takahashi, and H. Akagi, “A new neutral-point-clamped PWM inverter,” *IEEE Trans. Ind. Appl.*, vol. IA-17, no. 5, pp. 518–523, Sep. 1981.

[17] J. Birk and B. Andresen, “Parallel-connected converters for optimizing efficiency, reliability and grid harmonics in a wind turbine,” in *Proc. Eur. Conf. Power Electron. Appl.*, Sep. 2007, pp. 1–7.

[18] B. Andresen and J. Birk, “A high power density converter system for the Gamesa G10x 4.5 MW wind turbine,” in *Proc. Eur. Conf. Power Electron. Appl.*, Sep. 2007, pp. 1–8.

[19] H. S. Che, W. P. Hew, N. A. Rahim, E. Levi, M. Jones, and M. J. Duran, “A six-phase wind energy induction generator system with series-connected DC-links,” in *Proc. 3rd IEEE Int. Symp. Power Electron. Distrib. Gener. Syst.*, Jun. 2012, pp. 26–33.

[20] P. T. Huynh, P. J. Wang, and A. Banerjee, “An integrated permanent-magnet-synchronous generator–rectifier architecture for limited-speed-range applications,” *IEEE Trans. Power Electron.*, vol. 35, no. 5, pp. 4767–4779, May 2020.

[21] P. Huynh and A. Banerjee, “Active voltage-ripple compensation in an integrated generator-rectifier system,” in *Proc. IEEE Appl. Power Electron. Conf. Expo.*, Mar. 2019, pp. 3199–3206.

[22] K. Tan and S. Islam, “Optimum control strategies in energy conversion of PMSG wind turbine system without mechanical sensors,” *IEEE Trans. Energy Convers.*, vol. 19, no. 2, pp. 392–399, Jun. 2004.

[23] S. M. R. Kazmi, H. Goto, H. Guo, and O. Ichinokura, “A novel algorithm for fast and efficient speed-sensorless maximum power point tracking in wind energy conversion systems,” *IEEE Trans. Ind. Electron.*, vol. 58, no. 1, pp. 29–36, Jan. 2011.

[24] S. Li, T. A. Haskew, R. P. Swatloski, and W. Gathings, “Optimal and direct-current vector control of direct-driven PMSG wind turbines,” *IEEE Trans. Power Electron.*, vol. 27, no. 5, pp. 2325–2337, May 2012.

[25] C. Meyer, M. Hoing, A. Peterson, and R. W. De Doncker, “Control and design of DC grids for offshore wind farms,” *IEEE Trans. Ind. Appl.*, vol. 43, no. 6, pp. 1475–1482, Nov. 2007.

[26] J. Robinson, D. Jovcic, and G. Joos, “Analysis and design of an offshore wind farm using a MVDC grid,” *IEEE Trans. Power Del.*, vol. 25, no. 4, pp. 2164–2173, Oct. 2010.

[27] B. Wu and M. Narimani, *High Power Converters and AC Drives*, 2nd ed. Hoboken, NJ, USA: Wiley, 2016.

[28] J. G. Kassakian, M. F. Schlecht, and G. C. Verghese, *Principles Power Electronics*. Reading, MA, USA: Addison-Wesley, 1991.

[29] C. H. Houpis and M. Garcia-Sanz, *Wind Energy Systems: Control Engineering Design*. Boca Raton, FL, USA: CRC Press, 2012.

[30] C. Bak *et al.*, “The DTU 10-MW reference wind turbine,” in *Proc. Danish Wind Power Res.*, 2013, pp. 1–22.

[31] T. M. Jahns and W. L. Soong, “Pulsating torque minimization techniques for permanent magnet AC motor drives-a review,” *IEEE Trans. Ind. Electron.*, vol. 43, no. 2, pp. 321–330, Apr. 1996.

[32] K. Ahsanullah, R. Dutta, and M. F. Rahman, “Analysis of low-speed IPMMs with distributed and fractional slot concentrated windings for wind energy applications,” *IEEE Trans. Magn.*, vol. 53, no. 11, pp. 1–10, Nov. 2017.

[33] G. Sulligoi, A. Tessarolo, V. Benucci, A. M. Trapani, M. Baret, and F. Luise, “Shipboard power generation: Design and development of a medium-voltage DC generation system,” *IEEE Ind. Appl. Mag.*, vol. 19, no. 4, pp. 47–55, Jul. 2013.

[34] A. Damiano, I. Marongiu, A. Monni, and M. Porru, “Design of a 10 MW multi-phase PM synchronous generator for direct-drive wind turbines,” in *Proc. 39th Annu. Conf. IEEE Ind. Electron. Soc.*, Nov. 2013, pp. 5266–5270.